Applied Physics Letters

RESEARCH ARTICLE | MAY 09 2023

Strong coupling of localized surface plasmons and intermolecular vibration mode at terahertz frequencies

Chao-Wei Chen ; Le-Di Chen ; Cheng-Yao Li; Xiang-Yu Wu ; Qing Cai ; Ren-Hao Fan ; Dong-Xiang Qi ; Ru-Wen Peng ; Mu Wang

Appl. Phys. Lett. 122, 191705 (2023)
https://doi.org/10.1063/5.0141602

Strong coupling of localized surface plasmons and intermolecular vibration mode at terahertz frequencies

Cite as: Appl. Phys. Lett. **122**, 191705 (2023); doi: 10.1063/5.0141602
Submitted: 6 January 2023 · Accepted: 24 April 2023 ·
Published Online: 9 May 2023

View Online Export Citation CrossMark

Chao-Wei Chen,[1] Le-Di Chen,[1] Cheng-Yao Li,[1] Xiang-Yu Wu,[1] Qing Cai,[1] Ren-Hao Fan,[1] Dong-Xiang Qi,[1] Ru-Wen Peng,[1,a)] and Mu Wang[1,2,a)]

AFFILIATIONS

[1]National Laboratory of Solid State Microstructures, School of Physics, and Collaborative Innovation Center of Advanced Microstructures, Nanjing University, Nanjing 210093, China

[2]American Physical Society, Hauppauge, New York 11788, USA

[a)]Authors to whom correspondence should be addressed: rwpeng@nju.edu.cn and muwang@nju.edu.cn

ABSTRACT

Organic molecular vibrations, typically occurring in the terahertz (THz) regime, can resonate with a metastructure. A hallmark Rabi splitting occurs when the coupling strength is sufficiently strong. In this work, we observe the strong coupling of localized surface plasmons (LSPs) and intermolecular vibration mode at THz on a metasurface spin-coated with organic molecule α-lactose monohydrate. Excited by transverse-electric THz waves, dispersive localized surface plasmons interact with nondispersive intermolecular vibrations and form two vibro-polariton modes. The angle-resolved transmission spectra of the coupled system are detected by using a terahertz time-domain spectrometer, demonstrating an anti-crossing effect with a clear Rabi splitting. By retrieving the coupling strength and Hopfield coefficients of polariton bands from the measured data, we further verify that these two bands originate from the strong coupling between LSPs and molecular vibration mode. Moreover, we show that it is possible to implement molecular concentration sensing based on this strong coupling effect. This study demonstrates a unique approach to investigate vibro-polaritons at the terahertz regime and provides a testbed for future applications of strong coupling effects in chemical detection and biosensing.

Light–matter interactions could be categorized as weak and strong coupling regimes. When the energy-exchange rate of a coupled system is higher than the decay rates, this system is regarded as in a strong coupling regime.[1] The strong coupling effect has been achieved in many frequency ranges. For instance, employing planar cavities or nanostructures, photons could strongly couple with excitons in inorganic or organic semiconductors,[2–8] transition metal dichalcogenides,[9–11] or perovskite[12–14] and, thus, form exciton polaritons in visible frequencies. Since exciton polaritons inherit both features of photons and excitons, they are essential in solving some fundamental issues in Bose–Einstein condensation[15,16] and in realizing applications of all-optical transistors,[17,18] light-emitter diodes,[19,20] polariton lasers,[21,22] and even quantum photonic network.[23] The strong coupling has recently been observed in infrared and terahertz (THz) frequencies. For example, in the infrared wave range, the phonon polaritons formed in hexagonal boron nitride[24–26] and polymers[27,28] are promising candidates for developing ultrasensitive infrared spectroscopy. Meanwhile, the THz resonators could interact with phonon modes in perovskites,[29] nanocrystals,[30] and semiconductor quantum wells[31–34] at the strong coupling regime.

Terahertz wave usually possesses a frequency in the range of 0.1–10 THz, which is between high-frequency microwave and far-infrared radiation.[35–38] As the energy of terahertz waves corresponds to molecular interactions, such as hydrogen bonding, van der Waals interactions, and lattice interactions,[39] the terahertz spectroscopy becomes an excellent platform for examining the strong coupling between the optical cavity and molecular vibration. Recently, strong vibrational coupling between the vibrational mode of organic molecules and the optical modes of Fabry–Pérot cavities[40] or photonic crystal[41] has been observed, yet those systems have not yet been reduced to the subwavelength scale. This Letter reports on the strong vibrational coupling at the subwavelength scale via coupling a plasmonic metasurface with α-lactose monohydrate molecules at the terahertz regime. Excited by the transverse-electric illumination, we observe that the intermolecular vibration mode (IVM) of α-lactose monohydrate molecules strongly couples with the localized surface plasmons (LSPs) of the terahertz metasurface. Consequently, a clear Rabi splitting between the two vibro-polariton modes is identified in the angle-resolved transmission spectra, signifying the existence of strong coupling. By substituting a conventional cavity (e.g., multilayered distributed Bragg reflectors) with a metasurface, we provide a unique open-cavity system and demonstrate the vibrational strong coupling at the subwavelength scale. By comparing with the mirror cavity,[40] the plasmonic metasurface possesses subwavelength and open cavity features, whereas compared with a photonic crystal,[41] the plasmonic resonator presents subwavelength confinement. The investigations may have potential applications in polaritonic chemistry and biosensing at subwavelength.

The metasurface is composed of an array of metal rod antenna on a polyethylene terephthalate (PET) substrate (with a thickness of about 40 μm), as illustrated in Fig. 1(a). While the incident wave maintains the electric component along the long axis of antennas, the metasurface supports LSPs owing to the contribution of surface plasmons in the single antenna and near-field coupling with neighboring elements. We set the length, width, and height of each antenna as 150 μm, 50 μm, and 50 nm, respectively, with the period as 330 μm in both the x- and y-directions. Figure 1(b) shows the simulated transmission spectra of both the metasurface and single antenna in the terahertz region with the full-wave finite-difference time-domain (FDTD) approach. Here, we use a commercial software package (i.e., Lumerical FDTD Solution 8.0.1), where the periodic condition and the plane wave illumination are employed. As shown in Fig. 1(b), although no resonance occurs in a single antenna, an apparent dip appears in the transmission spectra of the metasurface with the excitation of transverse-electric (TE) incidence. In addition, the frequency corresponding to this dip decreases as the incident angle increases. For the normal incidence, the dip appears at 0.607 THz, and the dip shifts to 0.501 THz when the incident angle decreases to 40°. We also simulate the electric field distributions in the x–y and x–z planes at the resonance frequency in the scenario of normal incidence, as shown in Fig. 1(c). The electric field is strongly confined at the ends of the rod antenna, which confirms the dip in transmission spectra results from the excitation of LSP mode in the metasurface. Furthermore, we calculate the mode volume[42,43] as $V_m = \frac{\int \varepsilon(\boldsymbol{r})|\boldsymbol{E}|^2 dr}{\max\left(\varepsilon(\boldsymbol{r})|\boldsymbol{E}|^2\right)}$, where $\boldsymbol{E}$ is the electric field and $\varepsilon(\boldsymbol{r})$ is the dielectric constant. Considering that the unit cell

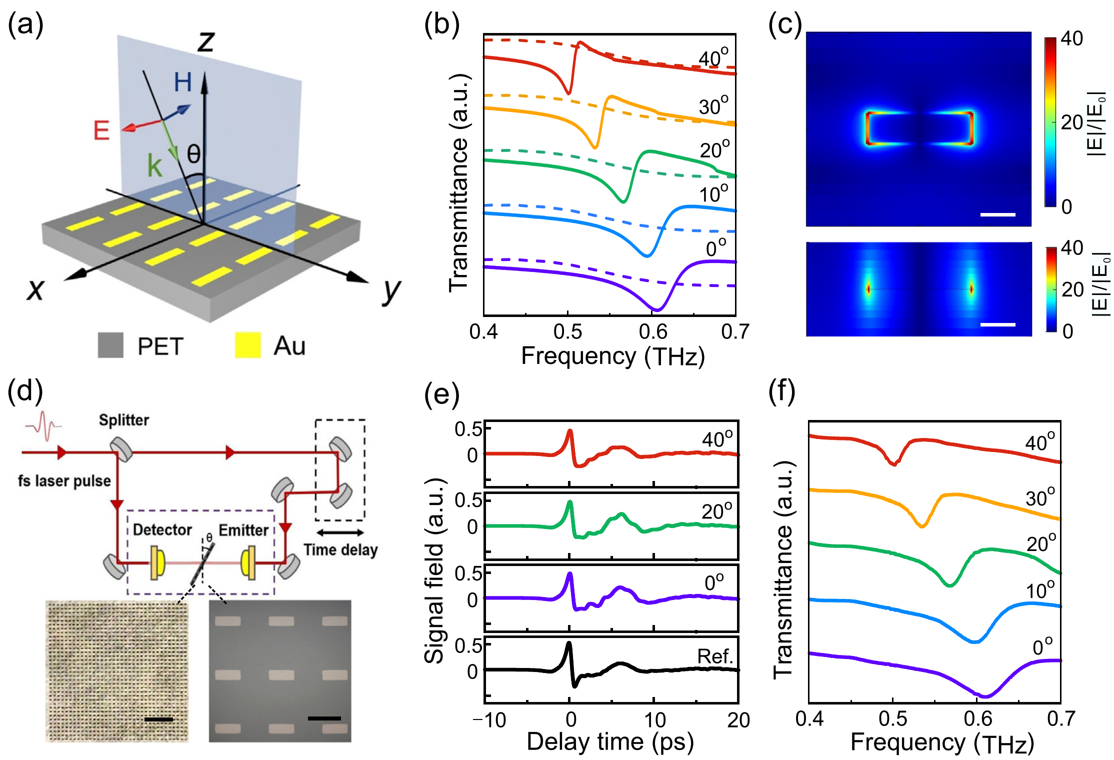

FIG. 1. (a) Schematic of the metasurface supporting localized surface plasmons (LSPs). In this study, the electric component of the incident wave is along the long axis of antennas. We define the incident plane where the magnetic component and incident wave vector lie, precisely the yz plane. The incident angle θ is the angle between the wave-vector k and z axis. (b) Simulated transmission spectra of the metasurface (solid curves) and single antenna (dashed curves) under different incident angles, respectively. (c) Electric field distributions of metasurface at the resonance frequency under normal incidence in the xy plane (upper) and xz plane (bottom). The upper and bottom scale bars both indicate 50 μm. (d) Upper: a schematic sketch of the terahertz time-domain spectrometer. The sample is placed in the area between the emitter and detector indicated by the purple dashed box, and the sample stage is rotated during measurement to obtain transmission data at different angles. Bottom: optical microscopic photographs of the metasurface sample, where the scale bars on the left and right insets indicate 2 mm and 200 μm, respectively. (e) Time-domain THz signals of reference (air) and metasurface sample under incident angles of 0°, 20°, and 40°. (f) Transmission spectra of the metasurface under different incident angles in 0°–40°.

in our designed metasurface has a physical volume of $330 \times 330 \times 180$ μm^3, we obtain the mode volume in a unit cell of the metasurface as $V_m \approx 2.08 \times 10^4\,\mu m^3$ at the resonant frequency of 0.61 THz (normal incidence), which is one order of magnitude smaller than that in the Fabry–Pérot cavity. Here, the mode volume in the Fabry–Pérot cavity is evaluated at the same integral physical volume ($330 \times 330 \times 180$ μm^3) and the same resonant frequency of 0.61 THz. This indicates that the presence of plasmonic metasurface indeed achieves better field confinement.

In experiments, the metasurface of the antenna array with the size of $1 \times 1\,cm^2$ is fabricated by photolithography and subsequently made with the metal deposition and liftoff processes. First, a layer of photoresist one micrometer in thickness is spin-coated on a PET substrate. The sample is then processed by photolithography. The exposed areas are removed by the developer. Next, a 50 nm-thick gold film is deposited on the sample using electron beam evaporation. Finally, via lifting-off, the antenna array metasurface is fabricated on the PET substrate. The top-view optical micrographs are shown at the bottom of Fig. 1(d), where both the size and the period of the antenna array are almost as designed. The optical measurements are carried out by a terahertz time-domain spectrometer (THz-TDS, EKSPLA/THZ, Lithuania), as schematically illustrated in the upper part of Fig. 1(d). Terahertz emitter and detector are both realized using photoconductive antennas. The terahertz emitter generates a linear polarized THz beam when excited by a femtosecond laser pulse with a central wavelength of 1560 nm. The illumination on the sample is a parallel THz wave with a spot diameter of 0.6 cm. The sample stage is rotated during the measurement [Fig. 1(d)] to obtain transmission signals at different incident angles. Then, the THz pulse is detected in the time domain using a probe laser beam from the same laser source with a varying pulse time delay relative to THz pulses. We first consider the time-domain signal of the air as the reference and then place the samples into the THz-TDS to obtain signals. Differences between the reference and samples could be observed in the time-domain signals after experiments with the TE illumination and different incident angles ranging from 0° to 40°, as illustrated in Fig. 1(e). The transmission spectra of the metasurface with varying angles of incidence are obtained using the fast Fourier transform (FFT), as shown in Fig. 1(f). The LSP dip redshifts from 0.609 THz at the normal incidence to 0.502 THz at the 40° incident angle. The experimental results are reasonably in agreement with the simulated ones. The background noise and inhomogeneity of the substrate may lead to a minor deviation.

Subsequently, we try to introduce the intermolecular vibration mode (IVM) of α-lactose monohydrate molecules into the system. Lactose ($C_{12}H_{22}O_{11}$) is a type of disaccharide combining one molecule of glucose and one molecule of galactose. It naturally exists in the milk of mammals and is widely used in infant foods, candies, margarine, and pills. One of its isomers, α-lactose, can be easily combined with a water molecule and forms an α-lactose monohydrate molecule. Similar to many biomolecules, the α-lactose monohydrate molecule has several characteristic absorption peaks at the terahertz regime, one of which occurs at approximately 0.53 THz,[44] and can be attributed to IVM of the hydrogen bond between the α-lactose molecule and crystal water. In our experiments, we first put 1500 mg α-lactose monohydrate into 2 ml PMMA solution to obtain an α-lactose suspension. Then, the lactose film with a thickness of 170 μm is spin-coated on a PET substrate with the α-lactose suspension. The micrograph of the α-lactose monohydrate film is shown in the inset of Fig. 2(a). Using THz-TDS, we measure the time-domain signal of this lactose film, as shown in Fig. 2(a). Also, the results after applying FFT are presented by the black curve in Fig. 2(b). The transmission spectra show a significant dip at 0.53 THz, which confirms the existence of IVM and agrees with previous studies.[44,45] The single Lorentzian oscillator model can be applied to fit the permittivity of the lactose film as follows:[46]

$$\varepsilon_L(\omega) = \varepsilon_\infty + \frac{f\omega_0^2}{\omega_0^2 - \omega^2 - i\Gamma\omega}, \tag{1}$$

where ε_∞ is the background permittivity of α-Lactose, ω_0 is the oscillator frequency, Γ is the damping constant, and f refers to the oscillator strength. The fitted parameters to achieve the best match with experimental results were $\varepsilon_\infty = 3.25$, $\omega_0 = 3.35 \times 10^{12}$ rad/s, $\Gamma = 6 \times 10^{10}$ rad/s, and $f = 0.0275$. The red curve in Fig. 2(b) shows the fitting result. A high oscillation strength and relatively small damping constant will guarantee the realization of the strong coupling between LSP and IVM. In addition, the dispersion curves and transmission spectra of α-lactose monohydrate molecules under different incident angles are measured, as illustrated in Figs. 2(c) and 2(d). Notably, IVM remains constant when the incident angle varies.

We cover the metasurface with the α-lactose monohydrate film to realize the strong coupling between LSP and IVM, as shown in Fig. 3(a). In the strong coupling regime, the original LSP and IVM disappear, but the upper polariton band (UPB) and lower polariton band (LPB) occur, as schematically presented in Fig. 3(b). We measure time-domain signals of the hybrid system in TE illumination with different incident angles. Figure 3(c) shows the two-dimensional dispersion map of the coupled system, in which the red and black curves indicate the new modes. As expected, two hybrid modes appear and disperse with varied incident angles. As shown in Fig. 3(c), there exist an evident anti-crossing phenomenon and a clear Rabi splitting between two modes, i.e., upper polariton band (UPB) and lower polariton band (LPB) have been formed due to the strong coupling effects. The anti-crossing phenomenon can be observed more directly in the angular-resolved transmission spectra, as presented in Fig. 3(d), where the dashed lines trace the vibro-polariton modes. Unlike the crossed original modes, the new modes separate at an incident angle of approximately 18°. Thus, the strong coupling between IVM from α-lactose monohydrate and LSP of the metasurface is realized in this system.

To analyze the strong coupling effects between IVM and LSP, we extract the frequencies of UPB and LPB at different incident angles, as presented in Fig. 4(a) with the blue and red dots, respectively. Figure 4(a) demonstrates that the dispersions represent the formation of vibro-polariton modes near the characteristic frequency of IVM, which is presented as the planar black dashed line. The interaction between the LSP and IVM in this system can be described by the mode-coupled Hamiltonian based on Jaynes–Cummings model,[47] i.e.,

$$\hat{\mathcal{H}} = h\nu_{LSP}\hat{a}^\dagger\hat{a} + h\nu_{IVM}\hat{b}^\dagger\hat{b} + h\nu_g\left(\hat{a}^\dagger\hat{b} + \hat{a}\hat{b}^\dagger\right), \tag{2}$$

$$h\begin{pmatrix} \nu_{LSP}(\theta) & \nu_g \\ \nu_g{}^* & \nu_{IVM} \end{pmatrix}\begin{pmatrix} \alpha_{LSP} \\ \alpha_{IVM} \end{pmatrix} = h\nu_p(\theta)\begin{pmatrix} \alpha_{LSP} \\ \alpha_{IVM} \end{pmatrix}, \tag{3}$$

where $\hat{a}(\hat{b})$ and $\hat{a}^\dagger(\hat{b}^\dagger)$ are the annihilation and creation operators of LSP (IVM), respectively, ν_{LSP} (ν_{IVM}) is the frequency of LSP (IVM),

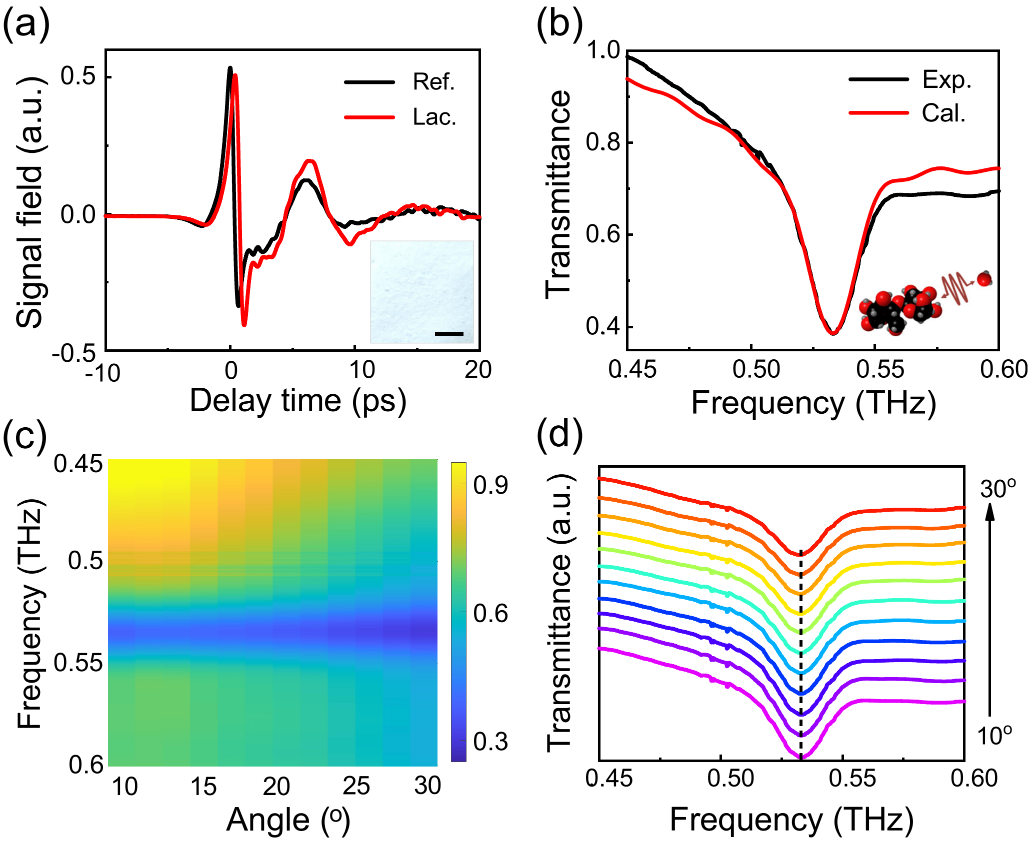

FIG. 2. (a) Time-domain signals of the α-lactose monohydrate film and reference. The inset shows a photograph of the α-lactose monohydrate film with a scale bar of 0.5 cm. (b) Black curve shows the experimental transmission spectra of the molecule α-lactose monohydrate film under the normal incidence, which satisfactorily agrees with the calculated results indicated by the red curve. The inset describes the vibration of the hydrogen bond between the α-lactose molecule and crystal water. (c) The two-dimensional dispersion map of the α-lactose monohydrate film under different incident angles (10°–30°). The color implies the value of transmittance. (d) The angle-resolved transmission spectra of the α-lactose monohydrate film under different incident angles (10°–30°).

ν_g is the coupling strength, and h is the Plank constant. For each incident angle, this model predicts the formation of two vibro-polariton modes, and each vibro-polariton mode can be written as

$$\left|P^{L(U)}\right\rangle = \alpha_{LSP}^{L(U)}\left|LSP\right\rangle + \alpha_{IVM}^{L(U)}|IVM\rangle, \tag{4}$$

where $|\alpha_{LSP}^{L(U)}|^2$ and $|\alpha_{IVM}^{L(U)}|^2$ are the Hopfield coefficients in each vibro-polariton mode. Thus, the polaritons inherit features of both the LSPs and molecule vibration modes. In this system, fitting results of the theoretical model satisfactorily agree with the measurement results when the coupling strength ν_g is 0.01 THz (i.e., the Rabi splitting is ∼0.02 THz). The blue and red curves in Fig. 4(a) represent the results of the theoretical model fitted to the measured data points. It is noted that the Rabi splitting in this plasmonic metasurface is less than that in the mirror cavity in Ref. 40. The main reason is that the coupling strength ($\nu_g \propto \sqrt{N}/\sqrt{V_m}$) strongly depend on not only the mode volume (V_m) but also the number of molecules (N). In our plasmonic sample, the thickness, area, and molecular concentration of the α-lactose layer are less than those in the mirror-cavity sample in Ref. 40. Therefore, it is less number of α-lactose molecules that leads to a smaller Rabi splitting in our plasmonic sample although better field confinement is achieved in the plasmonic sample.

Since many physical properties of polaritons are associated with Hopfield coefficients, such as the amplitude, full width at half-maximum (FWHM),[48] optical Stark effect,[3,11] the Hopfield coefficients should be determined. Based on the experimental and fitting results, we retrieve the Hopfield coefficients $|\alpha_{LSP}|^2$ and $|\alpha_{IVM}|^2$ in each vibro-polariton mode, as shown in Figs. 4(b) and 4(c). The upper polariton band is primarily composed of LSP at smaller incident angles. For example, UPB comprises approximately 90% of LSP and 10% of IVM when the incident angle is 10°. By increasing the incident angle, the Hopfield coefficient of LSP decreases, whereas the Hopfield coefficient of IVM increases. The IVM component continually increases until the incident angle reaches approximately 18°, where the Hopfield coefficients of LSP and IVM become equal. Subsequently, the Hopfield coefficient of IVM in UPB continues to increase toward unity at a reduced rate. Simultaneously, the LSP component in UPB diminishes to less than 5% at 30°. When the incident angle approaches 18°, where the Hopfield coefficients of LSP and IVM in UPB are equal, the Rabi splitting occur. In addition, the Hopfield coefficients in LPB possess a

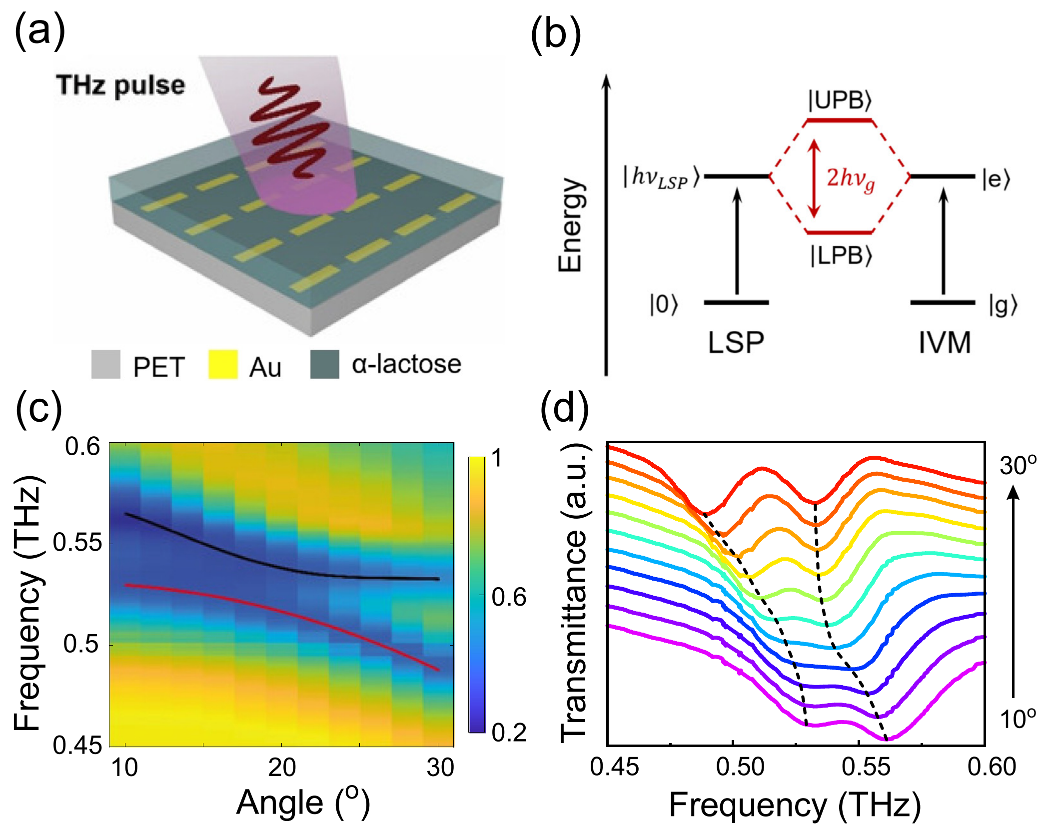

FIG. 3. (a) Schematic of the strongly coupled system comprising the PET substrate, the antenna array metasurface, and the α-lactose monohydrate film. (b) Interactions between LSP and IVM. (c) Two-dimensional dispersion map of the coupled system. The black and red curves indicate the upper polariton band (UPB) and lower polariton band (LPB), respectively. The color implies the value of transmittance. (d) Transmission spectra of the coupled system under different incident angles in the range of 10°–30°. The dashed lines trace the vibro-polariton modes.

similar trend; however, they increase with the LSP component and decrease with the IVM component.

It is worthwhile to mention the damping in our strong coupling system. As we know, the polariton modes[1] at resonance could be defined as $\omega_{\pm} = \omega_0 - \frac{i\gamma}{4} - \frac{i\gamma_{lsp}}{4} \pm \frac{1}{2}\sqrt{A - \frac{1}{4}\left(\gamma^2 - \gamma_{lsp}{}^2\right)^2}$, where ω_0 is the central frequency of the oscillator. Here, $A = \frac{Ne^2}{Vm\varepsilon_0}$, where m is mass, e is the electron charge, and N/V is the concentration of the α-lactose molecule. γ_{lsp} and γ are the damping factors of LSP and IVM, respectively, which can be extracted from the corresponding transmission spectra [i.e., Figs. 1(f) and 2(d)]. For example, $\gamma_{lsp} \approx 0.02$ THz and $\gamma \approx 0.02$ THz at the incident angle of 30°. Complex polariton modes $\omega_{\pm}$ are actually damped modes[1] with linewidths $\Delta\omega = \frac{\gamma}{2} + \frac{\gamma_{lsp}}{2} \approx 0.02$ THz, which is comparable to the Rabi splitting in this system. Moreover, the FWHM of the upper and lower polariton bands can be calculated based on the Hamiltonian with damping factors of modes.[48] As shown in Fig. 4(d), the calculated FWHM of the upper and lower polariton bands agrees reasonably with the measured ones directly from transmission spectra of strongly coupled metasurface system [as shown Fig. 3(d)] under incident angles 20°–30°.

Interestingly, a linear relationship between the coupling strength (ν_g) and the square root of the number of molecules could be expected in such a strongly coupled system. On the top of the metasurface, we now cover the α-lactose layer with seven different molecular concentrations (n) as 226, 304, 395, 492, 600, 766, and 900 mg/cm^3, respectively. The measured angle-resolved transmission spectra show both the UPB and the LPB in each sample. Then, we fit the measured polaritonic dispersions based on the Jaynes–Cummings model. Two typical examples are provided in Figs. 5(a) and 5(b) for the samples with $n = 304$ and 600 mg/cm^3, respectively. Thereafter, the coupling strength (ν_g) is achieved at different molecular concentrations (n). As shown in Fig. 5(c), we observe a linear relationship between ν_g and $n^{1/2}$ (i.e., $\nu_g \propto n^{1/2}$). This feature allows us to use plasmonic metasurfaces to detect molecule concentration (for example, α-lactose) and do the biosensing by tracing the frequency shift in the transmission spectra with molecular concentration variation. From Fig. 5(c), we find that the sensitivities defined as $\Delta\nu_g/\Delta n^{1/2}$ are about 5.49 GHz/(g$^{1/2}$/cm$^{3/2}$) in this metasurface-based sensor.

Realizing the strong coupling between LSP from plasmonic metasurfaces and IVM from α-lactose monohydrate molecules at the terahertz regime has a unique significance. It provides an open cavity to monitor the strong coupling system readily. For example, the formation of vibro-polaritons may tilt the reactivity landscape and monitor the chemical reaction rate[49–51] and promote the development of polaritonic chemistry. On the other hand, owing to reasonable

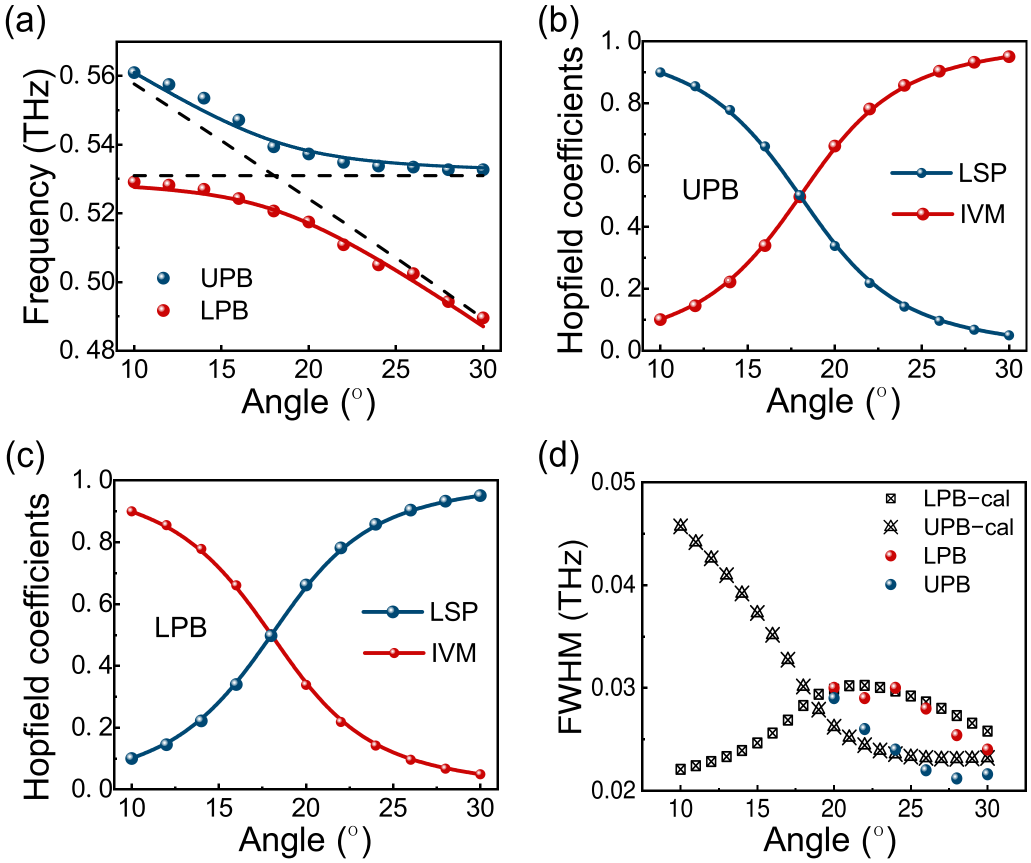

FIG. 4. (a) Fitting the measured polaritonic dispersion in the coupled system using the Jaynes–Cummings model. The blue and red dots show frequencies of the upper and lower polariton bands extracted from the experimental results. In contrast, the solid lines are achieved using the Hamiltonian of Jaynes–Cummings model. The black dashed lines represent the bare LSP (the oblique one) and IVM (the planar one), respectively. (b) and (c) The Hopfield coefficients of LSP and IVM in the upper and lower polariton bands, retrieved from the experimental and fitting results. (d) The full width at half-maximum (FWHM) of upper and lower polariton bands. The black triangles and squares represent calculated ones using the Hamiltonian with damping factors of modes. The blue and red dots represent the FWHM directly from the experiments [Fig. 3(d)], where the FWHM of resonant dips could be accurately identified under incident angles 20°–30°.

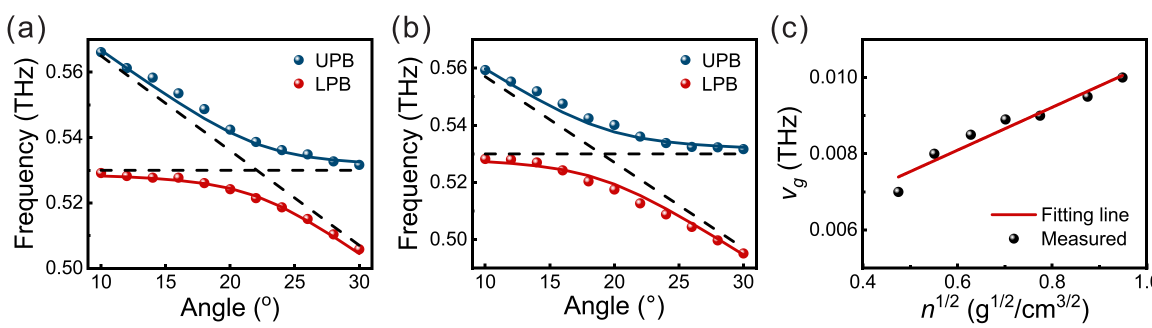

FIG. 5. Measured transmission spectrum and fitting results for the molecular concentration of (a) 304 and (b) 600 mg/cm^3. The blue and red dots show frequencies of the upper and lower polariton bands extracted from the experimental results. In contrast, the solid lines are achieved using the Hamiltonian of Jaynes–Cummings model. The black dashed lines represent the bare LSP (the oblique one) and IVM (the planar one), respectively. (c) Measured (black dots) and fitting (red line) coupling strength as the function of the square root of molecular concentration ($n^{1/2}$) in the samples with different molecular concentrations.

penetrability, broadband, and low energy, the terahertz wave has potential applications in biosensing and detecting. For instance, traditional molecular concentration sensors[52–54] are based on the frequency linearly shifting with a variation of the molecular concentration (n), which usually have high detection accuracy but a low measurement range. Compared to those traditional sensors, the metasurface sensing approach is based on the frequency linearly shifting with a variation of $n^{1/2}$, which provides a more extensive sensing range even though it compromises detection accuracy. We expect the strong coupling between terahertz metasurfaces and biomolecules to yield unique terahertz biosensors at the subwavelength scale.

In summary, we experimentally demonstrate the strong coupling between LSP and IVM of the antenna-array metasurface covered with α-lactose monohydrate molecules. Owing to the strong field enhancement effect of LSP in the metasurface and the large oscillation strength of IVM in α-lactose monohydrate molecules, convincing evidence of the strong coupling could be observed in the transmission spectra. Two vibro-polariton modes appear with variable incident angles, and an apparent Rabi splitting of 0.02 THz is observed at an incident angle of approximately 18°. In addition, we obtain a reasonable fitting to our experimental results with ν_g as 0.01 THz and retrieve the Hopfield coefficients of each vibro-polariton mode. Moreover, we demonstrate the possibility of molecular concentration sensing based on this strong coupling effect. This study provides a solid reference for exploring THz strong coupling effects at the subwavelength scale. The THz vibro-polariton modes have potential applications in polaritonic chemistry, biosensing, and detection.

This work was supported by the National Key R&D Program of China (Grant Nos. 2022YFA1404303 and 2020YFA0211300), the National Natural Science Foundation of China (Grants Nos. 12234010, 61975078, and 11974177), and partially by the Natural Science Foundation of Jiangsu Province (Grant No. BK20221438) and the Fundamental Research Funds for the Central Universities (Grant No. 020414380204).

AUTHOR DECLARATIONS

Conflict of Interest

The authors have no conflicts to disclose.

Author Contributions

Chao-Wei Chen: Data curation (equal); Formal analysis (equal); Investigation (equal); Methodology (equal); Validation (equal); Writing – original draft (equal). **Le-Di Chen:** Methodology (equal). **Cheng-Yao Li:** Formal analysis (equal); Validation (equal). **Xiang-Yu Wu:** Methodology (equal). **Qing Cai:** Formal analysis (equal). **Ren-Hao Fan:** Methodology (equal). **Dong-Xiang Qi:** Methodology (equal). **Ru-Wen Peng:** Conceptualization (equal); Formal analysis (equal); Funding acquisition (equal); Investigation (equal); Supervision (equal); Validation (equal); Writing – original draft (equal); Writing – review & editing (equal). **Mu Wang:** Formal analysis (equal); Funding acquisition (equal); Investigation (equal); Supervision (equal); Writing – review & editing (equal).

DATA AVAILABILITY

The data that support the findings of this study are available from the corresponding authors upon reasonable request.

REFERENCES

[1]P. Törmä and W. L. Barnes, Rep. Prog. Phys. **78**, 013901 (2015).
[2]D. G. Lidzey, D. D. C. Bradley, M. S. Skolnick, T. Virgili, S. Walker, and D. M. Whittaker, Nature **395**, 53 (1998).
[3]P. Vasa, W. Wang, R. Pomraenke, M. Maiuri, C. Manzoni, G. Cerullo, and C. Lienau, Phys. Rev. Lett. **114**, 036802 (2015).
[4]R. Chikkaraddy, B. de Nijs, F. Benz, S. J. Barrow, O. A. Scherman, E. Rosta, A. Demetriadou, P. Fox, O. Hess, and J. J. Baumberg, Nature **535**, 127 (2016).
[5]K. Zhang, W. B. Shi, D. Wang, Y. Xu, R. W. Peng, R.-H. Fan, Q. J. Wang, and M. Wang, Appl. Phys. Lett. **108**, 193111 (2016).
[6]K. Zhang, T. Y. Chen, W. B. Shi, C. Y. Li, R. H. Fan, Q. J. Wang, R. W. Peng, and M. Wang, Opt. Lett. **42**, 2834 (2017).
[7]V. C. Nikolis, A. Mischok, B. Siegmund, J. Kublitski, X. Jia, J. Benduhn, U. Hörmann, D. Neher, M. C. Gather, D. Spoltore, and K. Vandewal, Nat. Commun. **10**, 3706 (2019).
[8]L. Yang, X. Xie, J. Yang, M. Xue, S. Wu, S. Xiao, F. Song, J. Dang, S. Sun, Z. Zuo, J. Chen, Y. Huang, X. Zhou, K. Jin, C. Wang, and X. Xu, Nano Lett. **22**, 2177 (2022).
[9]X. Liu, W. Bao, Q. Li, C. Ropp, Y. Wang, and X. Zhang, Phys. Rev. Lett. **119**, 027403 (2017).
[10]C. Schneider, M. M. Glazov, T. Korn, S. Höfling, and B. Urbaszek, Nat. Commun. **9**, 2695 (2018).
[11]T. LaMountain, J. Nelson, E. J. Lenferink, S. H. Amsterdam, A. A. Murthy, H. Zeng, T. J. Marks, V. P. Dravid, M. C. Hersam, and N. P. Stern, Nat. Commun. **12**, 4530 (2021).
[12]T. Fujita, Y. Sato, T. Kuitani, and T. Ishihara, Phys. Rev. B **57**, 12428 (1998).
[13]W. Du, S. Zhang, Q. Zhang, and X. Liu, Adv. Mater. **31**, 1804894 (2019).
[14]R. Su, A. Fieramosca, Q. Zhang, H. S. Nguyen, E. Deleporte, Z. Chen, D. Sanvitto, T. C. H. Liew, and Q. Xiong, Nat. Mater. **20**, 1315 (2021).
[15]J. Kasprzak, M. Richard, S. Kundermann, A. Baas, P. Jeambrun, J. M. J. Keeling, F. M. Marchetti, M. H. Szymańska, R. André, J. L. Staehli, V. Savona, P. B. Littlewood, B. Deveaud, and L. S. Dang, Nature **443**, 409 (2006).
[16]T. Byrnes, N. Y. Kim, and Y. Yamamoto, Nat. Phys. **10**, 803 (2014).
[17]D. Ballarini, M. De Giorgi, E. Cancellieri, R. Houdré, E. Giacobino, R. Cingolani, A. Bramati, G. Gigli, and D. Sanvitto, Nat. Commun. **4**, 1778 (2013).
[18]A. V. Zasedatelev, A. V. Baranikov, D. Urbonas, F. Scafirimuto, U. Scherf, T. Stöferle, R. F. Mahrt, and P. G. Lagoudakis, Nat. Photonics **13**, 378 (2019).
[19]S. I. Tsintzos, N. T. Pelekanos, G. Konstantinidis, Z. Hatzopoulos, and P. G. Savvidis, Nature **453**, 372 (2008).
[20]J. Gu, B. Chakraborty, M. Khatoniar, and V. M. Menon, Nat. Nanotechnol. **14**, 1024 (2019).
[21]C. Schneider, A. Rahimi-Iman, N. Y. Kim, J. Fischer, I. G. Savenko, M. Amthor, M. Lermer, A. Wolf, L. Worschech, V. D. Kulakovskii, I. A. Shelykh, M. Kamp, S. Reitzenstein, A. Forchel, Y. Yamamoto, and S. Höfling, Nature **497**, 348 (2013).
[22]Q. Shang, M. Li, L. Zhao, D. Chen, S. Zhang, S. Chen, P. Gao, C. Shen, J. Xing, G. Xing, B. Shen, X. Liu, and Q. Zhang, Nano Lett. **20**, 6636 (2020).
[23]C. Qian, S. Wu, F. Song, K. Peng, X. Xie, J. Yang, S. Xiao, M. J. Steer, I. G. Thayne, C. Tang, Z. Zuo, K. Jin, C. Gu, and X. Xu, Phys. Rev. Lett. **120**, 213901 (2018).
[24]Y. Jia, H. Zhao, Q. Guo, X. Wang, H. Wang, and F. Xia, ACS Photonics **2**, 907 (2015).
[25]M. Barra-Burillo, U. Muniain, S. Catalano, M. Autore, F. Casanova, L. E. Hueso, J. Aizpurua, R. Esteban, and R. Hillenbrand, Nat. Commun. **12**, 6206 (2021).
[26]A. Bylinkin, M. Schnell, M. Autore, F. Calavalle, P. Li, J. Taboada-Gutièrrez, S. Liu, J. H. Edgar, F. Casanova, L. E. Hueso, P. Alonso-Gonzalez, A. Y. Nikitin, and R. Hillenbrand, Nat. Photonics **15**, 197 (2021).
[27]W. Ahn, I. Vurgaftman, A. D. Dunkelberger, J. C. Owrutsky, and B. S. Simpkins, ACS Photonics **5**, 158 (2018).
[28]K. S. Menghrajani, M. Chen, K. Dholakia, and W. L. Barnes, Adv. Opt. Mater. **10**, 2102065 (2022).
[29]H. S. Kim, N. Y. Ha, J.-Y. Park, S. Lee, D.-S. Kim, and Y. H. Ahn, Nano Lett. **20**, 6690 (2020).
[30]X. Jin, A. Cerea, G. C. Messina, A. Rovere, R. Piccoli, F. De Donato, F. Palazon, A. Perucchi, P. Di Pietro, R. Morandotti, S. Lupi, F. De Angelis, M. Prato, A. Toma, and L. Razzari, Nat. Commun. **9**, 763 (2018).

[31]M. Geiser, C. Walther, G. Scalari, M. Beck, M. Fischer, L. Nevou, and J. Faist, Appl. Phys. Lett. **97**, 191107 (2010).
[32]A. Tzimis, A. V. Trifonov, G. Christmann, S. I. Tsintzos, Z. Hatzopoulos, I. V. Ignatiev, A. V. Kavokin, and P. G. Savvidis, Appl. Phys. Lett. **107**, 101101 (2015).
[33]B. Paulillo, J.-M. Manceau, L. H. Li, A. G. Davies, E. H. Linfield, and R. Colombelli, Appl. Phys. Lett. **108**, 101101 (2016).
[34]A. Bayer, M. Pozimski, S. Schambeck, D. Schuh, R. Huber, D. Bougeard, and C. Lange, Nano Lett. **17**, 6340 (2017).
[35]B. Ferguson and X.-C. Zhang, Nat. Mater. **1**, 26–33 (2002).
[36]S. Zhang, J. Zhou, Y. Park, J. Rho, R. Singh, S. Nam, A. K. Azad, H. T. Chen, X. Yin, A. J. Taylor, and X. Zhang, Nat. Commun. **3**, 942 (2012).
[37]R. H. Fan, R. W. Peng, X. R. Huang, J. Li, Y. Liu, Q. Hu, M. Wang, and X. Zhang, Adv. Mater. **24**, 1980 (2012).
[38]R. H. Fan, Y. Zhou, X. P. Ren, R. W. Peng, S. C. Jiang, D. H. Xu, X. Xiong, X. R. Huang, and M. Wang, Adv. Mater. **27**, 1201 (2015).
[39]M. Walther, P. Plochocka, B. Fischer, H. Helm, and P. Uhd Jepsen, Biopolymers **67**, 310 (2002).
[40]R. Damari, O. Weinberg, D. Krotkov, N. Demina, K. Akulov, A. Golombek, T. Schwartz, and S. Fleischer, Nat. Commun. **10**, 3248 (2019).
[41]M. Kaeek, R. Damari, M. Roth, S. Fleischer, and T. Schwartz, ACS Photonics **8**, 1881 (2021).
[42]A. F. Koenderink, Opt. Lett. **35**, 4208 (2010).
[43]N. Lee, R. Kim, J. Y. Kim, J. B. Ko, S.-H. K. Park, S. O. Kim, M. L. Brongersma, and J. Shin, ACS Photonics **8**, 1616 (2021).
[44]E. R. Brown, J. E. Bjarnason, A. M. Fedor, and T. M. Korter, Appl. Phys. Lett. **90**, 061908 (2007).
[45]G. A. Komandin, K. I. Zaytsev, I. N. Dolganova, V. S. Nozdrin, S. V. Chuchupal, V. B. Anzin, and I. E. Spektor, Opt. Express **30**, 9208 (2022).
[46]E. Eizner and T. Ellenbogen, Appl. Phys. Lett. **104**, 223301 (2014).
[47]A. F. Kockum, A. Miranowicz, S. De Liberato, S. Savasta, and F. Nori, Nat. Rev. Phys. **1**, 19–40 (2019).
[48]K. Zhang, Y. Xu, T.-Y. Chen, H. Jing, W.-B. Shi, B. Xiong, R.-W. Peng, and M. Wang, Opt. Lett. **41**, 5740 (2016).
[49]A. Thomas, L. Lethuillier-Karl, K. Nagarajan, R. M. A. Vergauwe, J. George, T. Chervy, A. Shalabney, E. Devaux, C. Genet, J. Moran, and T. W. Ebbesen, Science **363**, 615 (2019).
[50]M. V. Imperatore, J. B. Asbury, and N. C. Giebink, J. Chem. Phys. **154**, 191103 (2021).
[51]K. Nagarajan, A. Thomas, and T. W. Ebbesen, J. Am. Chem. Soc. **143**, 16877 (2021).
[52]Y. Li, X. Chen, F. Hu, D. Li, H. Teng, Q. Rong, W. Zhang, J. Han, and H. Liang, J. Phys. D **52**, 095105 (2019).
[53]J. Yang, L. Qi, B. Li, L. Wu, D. Shi, J. A. Uqaili, and X. Tao, Results Phys. **26**, 104332 (2021).
[54]S. J. Park, J. T. Hong, S. J. Choi, H. S. Kim, W. K. Park, S. T. Han, J. Y. Park, S. Lee, D. S. Kim, and Y. H. Ahn, Sci. Rep. **4**, 4988 (2014).